



Geophysical Research Letters

RESEARCH LETTER

10.1029/2021GL093095

Key Points:

- Density irregularities occur near plasmapause due to alternating plasmasphere erosion and replenishment events during a geomagnetic storm
- Whistler waves exhibit a frequency modulation with higher-frequency waves at density troughs and lowerfrequency waves at density crests
- The amplitude of lower (higher) frequency whistler-mode waves is correlated (anti-correlated) with the relative plasma density variation

Correspondence to:

X. Liu and L. Chen, xu.liu1@utdallas.edu; lunjin.chen@gmail.com

Citation:

Liu, X., Gu, W., Xia, Z., Chen, L., & Horne, R. B. (2021). Frequency-dependent modulation of whistler-mode waves by density irregularities during the recovery phase of a geomagnetic storm. *Geophysical Research Letters*, 48, e2021GL093095. https://doi.org/10.1029/2021GL093095

Received 23 FEB 2021 Accepted 19 JUL 2021

Frequency-Dependent Modulation of Whistler-Mode Waves by Density Irregularities During the Recovery Phase of a Geomagnetic Storm

Xu Liu¹, Wenyao Gu¹, Zhiyang Xia¹, Lunjin Chen¹, and Richard B. Horne²

¹William B. Hanson Center for Space Sciences, University of Texas at Dallas, Richardson, TX, USA, ²British Antarctic Survey, Cambridge, UK

Abstract Density irregularities near the plasmapause are commonly observed and play an important role in whistler-mode wave excitation and propagation. In this study, we report a frequency-dependent modulation event of whistler-mode waves by background density irregularities during a geomagnetic storm. Higher-frequency whistler waves (near $0.5\ f_{ce}$, where f_{ce} is the equatorial electron cyclotron frequency) are trapped in the density trough regions due to the small refractive index near the parallel direction, while lower-frequency whistler waves (below $0.02\ f_{ce}$) are trapped in the density crest regions due to the refractive index maximum along the parallel direction. In addition to the modulation, we also find that, quantitatively, the wave amplitude of the higher- (lower-) frequency whistler-mode waves is anti-correlated (correlated) with the relative plasma density variation. Our study suggests the importance of density irregularity dynamics in controlling whistler-mode wave intensity, and thus radiation belt dynamics.

Plain Language Summary Whistler-mode waves play important roles in controlling the dynamics of the Earth's radiation belts. Whistler-mode chorus waves are responsible for pitch-angle scattering of energetic electrons and the resulting formation of diffuse aurora at L < 8. Density irregularities near the plasmapause affect the plasma wave excitation and propagation. In this study, we find five density irregularity events during a geomagnetic storm from 14 to 19 October 2013 based on the twin Van Allen Probes. We report a frequency-dependent modulation of whistler-mode waves by background density irregularities on October 18, 2013. By an instability analysis and a ray-tracing simulation, we demonstrate that higher-frequency whistler-mode waves are trapped in density troughs due to the small refractive index near the parallel direction, while lower-frequency whistler-mode waves are trapped in density crests due to the refractive index maximum along the parallel direction. We also show that wave amplitude of higher- (lower-) frequency whistler-mode waves is highly anti-correlated (correlated) with the relative density variation. This study shows that density irregularities are of great importance to the occurrence, frequency range, and amplitude of whistler-mode waves and should be taken into account when modeling whistler-mode waves in the magnetosphere.

1. Introduction

The plasmasphere is a vast torus-shaped region in the inner magnetosphere filled with dense $(\sim 10^2-10^6~\text{H/cm}^3)$ and cold (less than 10 eV) ions and electrons. Controlled by the co-rotation and convection electric fields, plasmasphere erosion and refilling occur regularly due to the increase and decrease in geomagnetic activities, respectively (Carpenter & Anderson, 1992; Darrouzet et al., 2013; Grebowsky, 1970). The outer boundary of the plasmasphere, called plasmapause, is a sharp plasma density boundary that separates the closed and open drift paths for cold plasma. Due to the dramatic variation of the plasma properties across the plasmapause (Liu, Chen, & Xia, 2020), the plasmapause plays a crucial role in determining energetic and relativistic particle distributions (Lorentzen et al., 2001) and controlling the growth and propagation of various electrostatic and electromagnetic emissions in the inner magnetosphere (Liu et al., 2015, and reference therein). For example, as shown by satellite observations and numerical simulations, electron cyclotron harmonic (ECH) waves (e.g., Horne et al., 2013; Liu, Chen, Engel, & Jordanova, 2020; Liu, Chen, & Xia, 2020; Ma et al., 2016; Meredith et al., 2009, and references therein), and whistler-mode chorus waves (e.g., Jordanova et al., 2010; Li et al., 2009; Santolík et al., 2004, and references therein) usually occur

© 2021. American Geophysical Union. All Rights Reserved.

LIU ET AL. 1 of 10



outside the plasmapause, while plasmaspheric hiss waves often occur inside the plasmasphere (e.g., Cao et al., 2005; Chen et al., 2012a, 2012b; Thorne et al., 1973; Yu et al., 2017, and references therein).

However, distinct plasmapauses with a sharp density variation account for only 16% of all plasmapause crosses observed by the Combined Release and Radiation Effects Satellite (CRRES) (Moldwin et al., 2002) and occur preferentially at the post-midnight and dawnside (with an occurrence rate of > 50%) rather than the duskside (with an occurrence rate of < 45%) in the Time History of Events and Macroscale Interactions during Substorms (THEMIS) satellite observations (from Figure 2 of Liu et al., 2015). Most plasmapauses, however, are accompanied by significant density irregularities (Carpenter et al., 2000; Darrouzet et al., 2004; Kazama et al., 2018; Moldwin et al., 2002), which are thought to play an important role in controlling wave excitation and propagation, such as the excitation of electromagnetic ion cyclotron (EMIC) (Chen et al., 2009; Yue et al., 2020) and magnetosonic (MS) waves (Yue et al., 2020) and the propagation of EMIC (Yuan et al., 2019) and MS waves (Liu et al., 2018; Ma et al., 2014; Yuan et al., 2019).

In this study, we use twin Van Allen Probes (VAPs) to demonstrate a distinct frequency-dependent modulation of whistler-mode waves by density irregularities near the plasmapause. The organization of this study is as follows. The dynamics of the plasmasphere and accompanying density irregularities during a geomagnetic storm are shown in Section 2. In Section 3, a frequency-dependent modulation event of whistler-mode waves by density irregularities is presented, followed by an instability analysis for this modulation event. In Section 4, a wave propagation analysis for this modulation event is performed by a dispersion relation analysis and a ray-tracing simulation. A quantitative relation between wave amplitude and relative density variation of the density irregularities is shown in Section 5, followed by the conclusion and discussion in Section 6.

2. Plasmasphere Dynamics and Density Irregularities During a Geomagnetic Storm

Figures 1a-1c show the Kp, AE, and Dst indices from 14 to 19 October 2013. A geomagnetic storm started approximately 8 h after 00:00 UT on October 14, 2013 (t_0), and the Dst index reached a minimum approximately 27 h after t₀. Then, the storm took the next 4–5 days to recover. During the main phase, the Kp and AE indices were greatly enhanced with peak values above 4 and 800 nT, respectively. Several substorms occurred during the recovery phase, as indicated by the peaks of the AE index (also see supporting information of Forsyth et al., 2015). During this storm event, VAP-A (black lines in Figure 1d) and VAP-B (red lines in Figure 1d) passed a similar spatial region 16 times (indicated by gray and red shading regions in Figures 1a-1c, respectively), with an L shell from 6 to 2 and magnetic local time (MLT) from 17 to 23 over their consecutive inbound orbits (Figure 1d). Plasma density inferred from the measured upper hybrid resonant (UHR) frequency by the high-frequency receiver (HFR) (Kletzing et al., 2013) of VAP-A during these 16 inbound orbits is shown in Figure 1e as a function of orbit sequence and L shells. A black contour of $100 \# / cm^3$ is added as a reference to indicate the plasmasphere dynamics (erosion and refilling). Six erosions (Orbits 1 to 3, Orbits 4 to 5, Orbits 6 to 7, Orbits 9 to 11, Orbits 13 to 14, and Orbits 15 to 16) and five refillings (Orbits 3 to 4, Orbits 5 to 6, Orbits 7 to 9, Orbits 11 to 13, and Orbits 14 to 15) occurred during this storm event. Figures 1f-1k show the detailed plasma density profiles (solid lines for VAP-A and dashed lines for VAP-B) on these 16 inbound orbits as a function of the L shell and universal time.

Four density irregularity events (indicated by black arrows in Figures 1g-1i, and 1k) can be found near the plasmapause (Orbits 4, 6, and 14) or the plume (Orbit 10) by at least one VAP. By comparing the plasma density profiles over these consecutive orbits, one event occurs near the plume (Figure 1i) during plasmasphere erosion, while the other three events (Figures 1g, 1h, and 1k) occur during either plasmasphere erosion or refilling.

Another event with significant density irregularities (where the density variation is comparable to the background density) can be found near the plasmapause on Orbit 12 (indicated by a red arrow in Figure 1j) when the plasmasphere undergoes refilling following a prior erosion (due to the increased AE index near 88 h after t_0). Associated with this large density irregularity event, whistler-mode waves with different frequencies are modulated in a different way, which will be shown in the next section.

LIU ET AL. 2 of 10

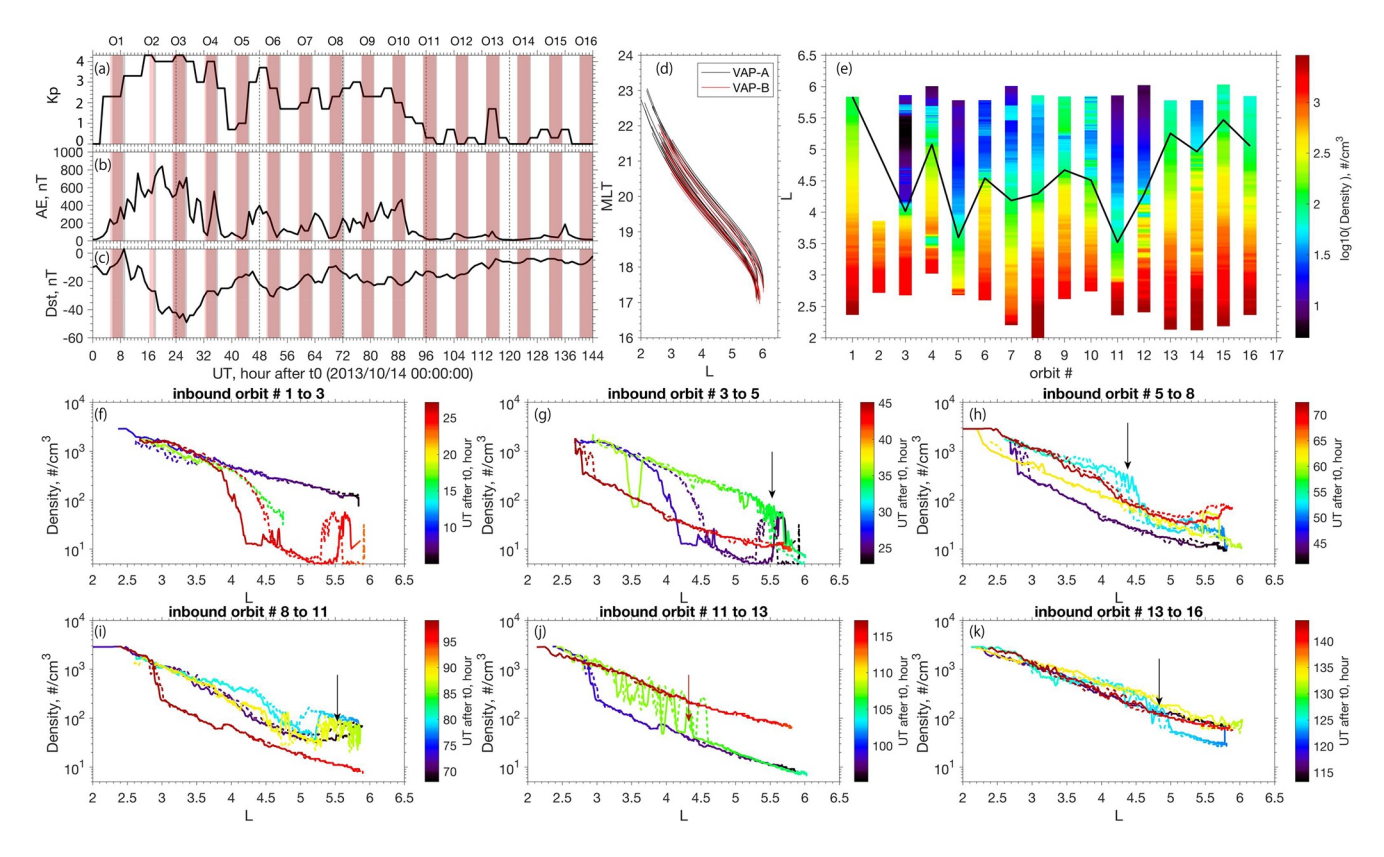


Figure 1. Plasma density observed by the twin Van Allen Probes (VAPs) on their 16 consecutive inbound orbits from 14 to 19 October 2013. (a) Kp, (b) AE and (c) Dst indices. Gray (VAP-A) and red (VAP-B) shading regions indicate time intervals of the inbound orbits of two VAPs. (d) L and MLT of 16 inbound orbits of VAP-A (black) and VAP-B (red). (e) Plasma density as a function of orbit number and L for VAP-A. The black contour indicates 100 #/ cm³ of each orbit. (f–k) Detailed plasma density as a function of L and universal time after 00:00 UT October 14, 2013 with orbit number shown in the title. Four black arrows indicate four density irregularity events, and one red arrow indicates a density irregularity event where the density variation is comparable to the background density.

3. Two Whistler-Mode Wave Modulations With Background Plasma Density and Instability Analysis

Figure 2 shows a frequency-dependent modulation event of whistler-mode waves by background plasma density during 11:06-11:48 UT (11.1-11.8 UT) on October 18, 2013, observed by VAP-A. Figure 2a shows the HFR electric field spectrum. A clear and highly perturbed upper hybrid resonant frequency line can be found above equatorial electron cyclotron frequency f_{ce} (the white solid line), and thus, plasma density can be derived (the black line in Figure 2e). Two types of whistler-mode waves can be found with strong wave electric (Figure 2b) and magnetic (Figure 2c) field power spectral densities and small wave normal angles (less than 40° in Figure 2d), observed by a waveform receiver (WFR) (Kletzing et al., 2013). Higher-frequency whistler-mode waves with wave frequencies of approximately $0.5 f_{ce}$ (denoted by white dashed lines in Figures 2b-2d) occur in density valleys and disappear in density crests. Lower-frequency whistler-mode waves with wave frequencies centered near 150 Hz and below the equatorial lower hybrid resonant frequency (denoted by white dotted-dashed lines in Figures 2b-2d) occur in density crests, and disappear in density valleys. Figure 2f shows the wave magnetic field amplitude of lower-frequency whistler-mode waves over the frequency range from 100 to 1,000 Hz (red) and higher-frequency whistler-mode waves over the frequency range 4-11 kHz (blue). Then, we can find that peak values of the wave amplitude of lower- (higher-) frequency whistler-mode waves, marked by red (blue) circles in Figure 2f, coincide with the corresponding plasma density peaks (valleys), marked by red (blue) circles in Figure 2e. This comparison demonstrates that the wave amplitude of lower- (higher-) frequency whistler-mode waves is correlated (anti-correlated) with the plasma density variation. To examine the quantitative relation between the whistler-mode wave amplitude and density variation, which will be shown later in Section 5, a lower envelope line (a red line in Figure 2e) and an upper envelope line (a blue line in Figure 2e) for the plasma density are identified via eye

LIU ET AL. 3 of 10

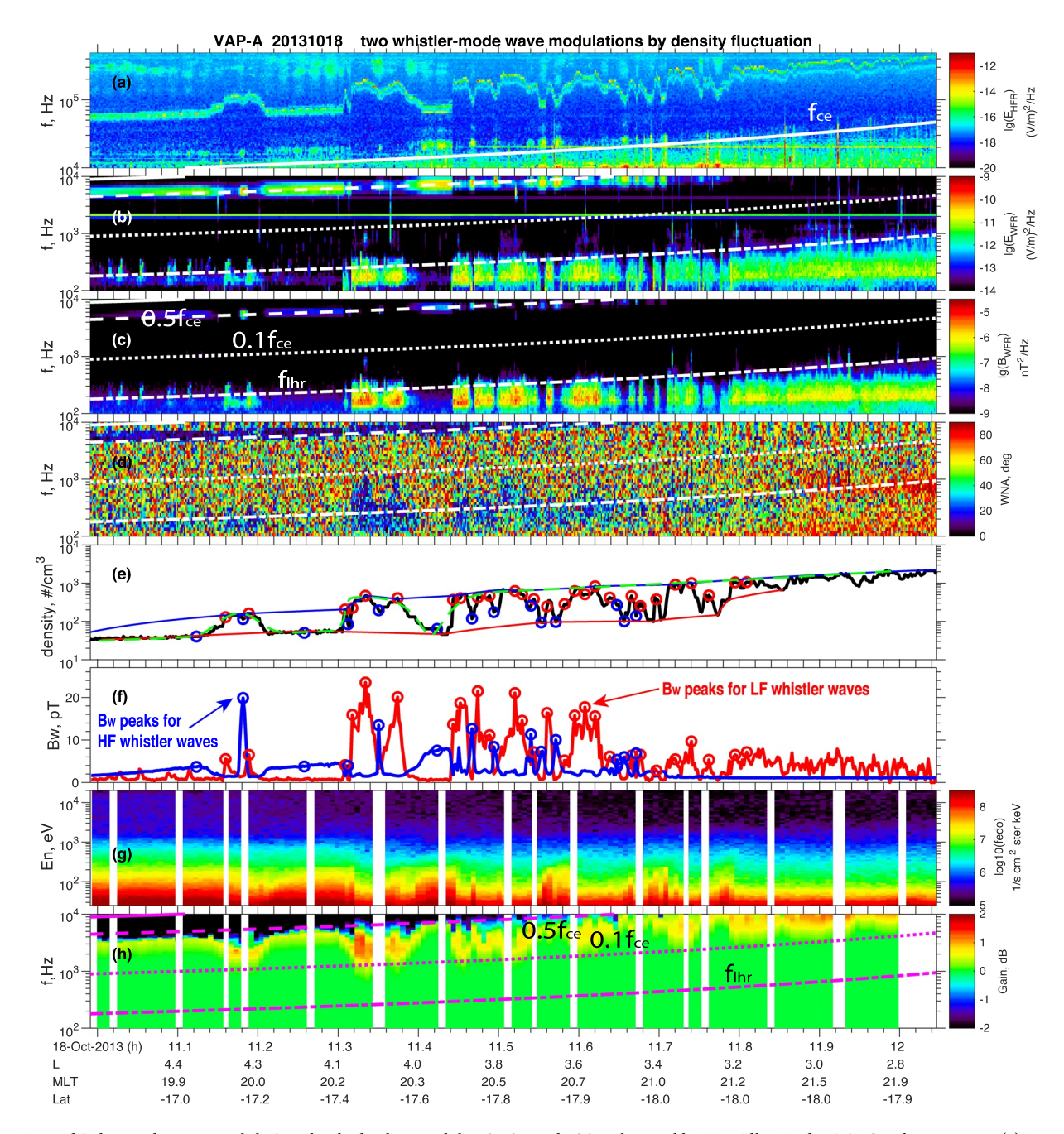


Figure 2. Two whistler-mode wave modulations by the background density irregularities observed by Van Allen Probe-A in October 18, 2013. (a) Burst high-frequency receiver spectrum. (b) Electric and (c) magnetic field spectra of waveform receiver (WFR). (d) Wave normal angle derived from the WFR magnetic field spectrum. (e) Plasma density derived from the upper hybrid resonant frequency. The green dashed line indicates the modeled density used in ray-tracing simulations. A red (blue) line indicates the lower (upper) envelope line of the plasma density. (f) Wave magnetic field amplitude of lower-frequency (LF) whistler waves (red) and higher-frequency (HF) whistler waves (blue). (g) Electron omnidirectional differential flux observed by HOPE. (h) Wave gains of the whistler-mode waves. The white solid line indicates the equatorial electron cyclotron frequency f_{ce} . The white and magenta dashed, dotted and dotted-dashed lines indicate $0.5 f_{ce}$, $0.1 f_{ce}$, and equatorial lower hybrid frequency, respectively. The red (blue) circles in (f) indicate the peak values of the wave magnetic field amplitude of LF (HF) whistler-mode waves and the corresponding plasma density in (e).

inspection by connecting local minima and maxima of the plasma density, respectively, showing that the density along the two envelope lines increases monotonously as the satellite moves inward.

To understand the correlation (anti-correlation) between the lower- (higher-) frequency whistler-mode waves and plasma density, we perform a wave instability analysis (wave gain) here and a propagation

LIU ET AL. 4 of 10



analysis in the next section to address the wave excitation and propagation effects, respectively. Here, wave gain in units of dB is used to describe the relative change in wave power on a logarithmic scale (e.g., 10 dB corresponds to a wave power enhancement by one order of magnitude) when the wave propagates from one location to another. To calculate the wave gain of whistler-mode waves, the K_i component of the convective growth rate \mathbf{k}_i , which is along the group velocity and contributes to convective amplification along a wave path, is calculated by $K_i = \gamma / |\mathbf{v}_p|$ (Chen et al., 2010), where \mathbf{v}_p is the group velocity and γ is the temporal growth rate calculated by Equation 6 in Liu and Chen (2019). For the γ calculation, following He et al. (2019), a function $F_e = P_1 exp(P_2 sin^2 \alpha)$ is used to fit the phase space density for each energy channel from 25 eV to 51 keV observed by the helium, oxygen, proton, and electron (HOPE) mass spectrometer (Funsten et al., 2014), where α is the electron pitch angle and P_1 and P_2 are two fitting parameters. The wave normal angle is set as 0° and wave gain is estimated based on a propagation path from the magnetic equator $(\lambda = 0^{\circ})$ to $\lambda = 20^{\circ}$ (satellite location), where λ is magnetic latitude. Figure 2g shows the electron omnidirectional differential flux observed by HOPE. Figure 2h shows the calculated wave gain during this event. Positive wave gain is in density crests with a small peak value of $\sim 2 dB$ between 0.1 f_{ce} (denoted by a magenta dotted line) and $0.5 f_{ce}$ (denoted by a magenta dashed line). Higher-frequency whistler-mode waves are damped or weakly amplified, as suggested by negative wave gain above 0.5 f_{ce} and small positive wave gain below 0.5 f_{ce} . Lower-frequency whistler-mode waves are not damped or amplified, corresponding to $\sim 0 dB$ wave gain. Thus, the small wave gains (≤2 dB) suggest that these frequency-dependent whistler-mode waves are not locally generated, while the observed wave intensity enhancement may be due to propagation confinement by density variations, as explained in the next section.

4. Propagation Effect of Whistler-Mode Waves by Density Irregularities

Following the suggestion at the end of Section 3, we investigate the whistler-mode wave propagation effect in this section. Figure 3a shows the wave refractive index surface $(n_{\perp} \text{ vs. } n_{*})$ using the cold plasma dispersion relation with the observed electron density and background magnetic field at UT = 11.2, where $n_{\perp} = \frac{ck_{\perp}}{c}$ and $n_{\parallel} = \frac{ck_{\parallel}}{c}$ are components of the refractive index vector in the perpendicular and parallel directions, respectively. c is the speed of light, k is the wavenumber, and ω is the wave frequency. For a wave refractive index surface at a given wave frequency, for example, 150 Hz (the red curve in Figure 3a), a vector (denoted by a black arrow labeled by V_n from the original point to any point on the surface represents the reciprocal of the normalized wave phase velocity (by c). Wave group velocity is perpendicular to the surface. The black arrow labeled by V_a indicates the direction of the group velocity. The wave normal angle (WNA) is the angle between the magnetic field direction and phase velocity. For the wave frequency between the lower hybrid resonant frequency f_{lhr} ($\approx 0.02 f_{ce}$) and $0.5 f_{ce}$, the wave refractive index surface looks like a "W" shape, such as the wave surface for $0.1 f_{ce}$ (the green curve in Figure 3a). The WNAs corresponding to the two minima of n_{ij} (at two wells of "W") are called Gendrin angles (GAs), at which the group velocity is along the parallel direction. The GA decreases from 90° to 0° when the wave frequency increases from f_{lhr} to $0.5 f_{ce}$. Then, the wave surface becomes a "U" shape with a single well near the parallel direction. In a uniform magnetic field, a density crest can lead to wave trapping near the maximum n_a of the wave refractive index surface (for the wave with frequency $f < 0.5 f_{ce}$), while a density valley can lead to wave trapping near the minimum n_{ij} of the wave refractive index surface (for the wave with frequency $f \ge 0.5 f_{co}$). This has been explained by Smith et al. (1960) based on Snell's law.

Figures 3b and 3c show ray-tracing simulations of whistler-mode waves (Horne, 1989) (with the five frequencies shown in Figure 3a) inside a density crest and a density trough, respectively. The setup of ray-tracing simulation is as follows. (a) The density model (indicated by gray color in Figures 3b and 3c) follows Bortnik et al. (2011). It is based on a diffusive equilibrium model with model parameters defined in Equations 1–5 of Bortnik et al. (2011) ($T_{DE}=1100~K$ and $N_b=3000~\#/~cm^3$). A plasmapause ($L_p=4.12, w=0.01, a=1.5,$ and $R_c=6500~km$), a one-side duct ($d_d=4, L_d=1.1,$ and $W_d=2.55$), a trough ($d_d=-0.92, L_d=3.96,$ and $W_d=0.07$), and a crest ($d_d=2.7, L_d=4.33,$ and $W_d=0.04$) are added to fit the measured electron density. The other parameters, which are not shown here, are the same as those for the modeled dayside plasmasphere in Bortnik et al. (2011). The modeled plasma density along the satellite trajectory is shown by a green

LIU ET AL. 5 of 10

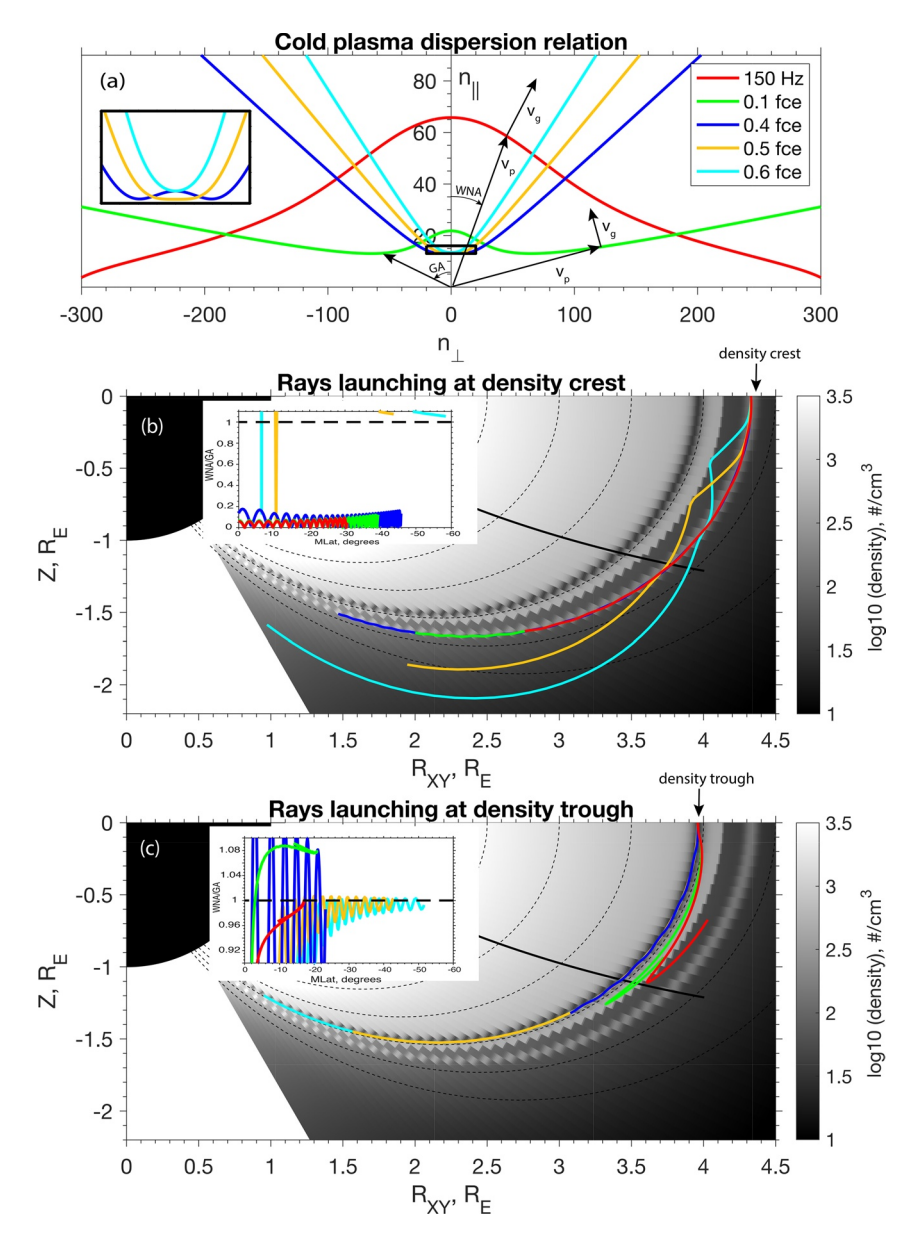


Figure 3. (a) Wave refractive index surfaces for different wave frequencies by using the cold plasma dispersion relation. Ray-tracing simulations with five rays launching at (b) L = 4.33 (center of outer density crest) and (c) L = 3.96 (center of density trough) from the magnetic equator with the launched frequency shown in panel (a). The gray colormap indicates the plasma density. The black solid lines indicate the trajectory of Van Allen Probe A (VAP-A). The quarter of the black sold sphere indicates the Earth. The small panels in panels (b) and (c) show the ratio of wave normal angles (WNAs) to Gendrin angles (GAs) corresponding to each ray as a function of the geomagnetic latitude.

dashed line in Figure 2e. (b) A dipole magnetic field model is used. (c) Five rays are launched from the magnetic equator at the center of the outer density crest (L=4.33) in Figure 3b and at the center of the density trough (L=3.96) in Figure 3c. The initial WNA is set as 5°. The satellite trajectory is denoted by a black solid line.

In Figure 3b, rays with frequencies less than $0.5\,f_{ce}$ (red, green, and blue rays) are ducted inside the density crest. The corresponding WNAs are much less than GAs (as shown in the small panel of Figure 3b), and thus, these rays are trapped near the parallel direction by the density crest (Smith et al., 1960). The rays with frequencies equal to and above $0.5\,f_{ce}$ (yellow and cyan rays) do not experience ducting. Instead, their

LIU ET AL. 6 of 10



wave normals are refracted outward (to larger L shells), but the rays propagate inward (to smaller L shells) because of opposite perpendicular directions of the group velocity and phase velocity at those frequencies.

In Figure 3c, rays with frequencies equal to and larger than $0.4 f_{ce}$ (blue, yellow, and cyan rays) are ducted inside the density trough. According to the theory of Smith et al. (1960), in the uniform magnetic field, whistler-mode waves above 0.5 f_{re} can be trapped by density valleys, while whistler-mode waves below $0.5 f_{re}$ can be trapped by density crests. However, the observation shows that wave intensity with frequency just below $0.5f_{ce}$ (Figures 2b and 2c) can also be enhanced in density trough regions, supporting these waves trapping in density troughs (blue ray in Figure 3c). The discrepancy between Smith's theory and ray tracing simulations is because of the dipole magnetic field and small GAs for these waves (see the zoomed-in part in Figure 3a). As waves propagate away from the equator, the dipole magnetic field tends to refract waves outward from the initial field line. As a consequence, the waves become oblique, and their WNAs surpass the GAs (blue, yellow, and cyan lines in the small panel in Figure 3c). The wave refractive index surface (for example, for 0.4 f_{re} in Figure 3a) exhibits a local n_{\parallel} maximum along the parallel direction and local n_{\parallel} minima along GAs. However, the surface essentially behaves as a well shape over a finite WNA range because the local n_{\parallel} maximum along the parallel direction is very close to the local n_{\parallel} minima along GAs, leading to effective wave trapping in density troughs. The rays with frequencies much smaller than 0.5 f_{req} (red and green rays in Figure 3c) propagate away from the density trough region and are reflected back to the magnetic equator because both the wave normal and group velocity of these waves are bent away from the density trough region (due to Snell's law).

5. Wave Amplitude and Relative Density Variation

In addition to explaining the frequency-dependent modulation of whistler-mode waves, we will examine the quantitative relation between the whistler-mode wave amplitude and relative density variation in this section. As shown in Section 3, two envelope lines of plasma density are denoted by red and blue lines in Figure 2e, respectively. Thus, the relative density variations $\frac{Ne - Ne_{base}}{Ne_{base}}$ and $\frac{Ne_{top} - Ne}{Ne_{top}}$ can be calculated, respectively, where Ne is the measured plasma density corresponding to the lower- (higher-) frequency whistler-mode waves (red and blue circles in Figure 2e), Ne_{base} is the plasma density along the lower envelope line, and Ne_{top} is the plasma density along the upper envelope line.

A quantitative relation between peak values of lower-frequency whistler-mode wave amplitude and the crest-associated relative density variation ($(Ne-Ne_{base})$ / Ne_{base}) is shown in Figure 4a (red circles) and then linearly fitted (the red line in Figure 4a). The correlation coefficient between the two parameters is 0.6672, and the 95% confidence interval of the fitting slope ranges from 1.05 to 2.83, suggesting that the amplitude of the lower-frequency whistler-mode waves is positively correlated with the relative density variation. Similarly, a quantitative relation between peak values of higher-frequency whistler-mode wave amplitude and trough-associated relative density variation ($(Ne_{top}-Ne)$ / Ne_{top}) is shown in Figure 4b (blue circles) and then linearly fitted (the blue line in Figure 4b). The correlation coefficient between the two parameters is -0.6248, and the 95% confidence interval of the fitting slope ranges from -30.54 to -3.66, suggesting that the amplitude of the higher-frequency whistler-mode waves is anti-correlated with the relative density variation.

These two clear relationships of the wave amplitude and relative density variation in Figure 4 show that in addition to effectively trapping whistler-mode waves, density irregularities can quantitatively control the whistler-mode wave amplitude.

6. Conclusion and Discussion

In this study, we have shown that density irregularities occur near the plasmapause when the plasmasphere experiences alternating erosions and refillings during the recovery phase of a geomagnetic storm event from 14 to 19 October 2013. During plasmasphere refilling after a substorm, density irregularities modulate whistler-mode wave intensity differently for different frequencies. We have performed an instability analysis and a propagation analysis to explain the modulation. Our principal conclusions are summarized as follows:

LIU ET AL. 7 of 10

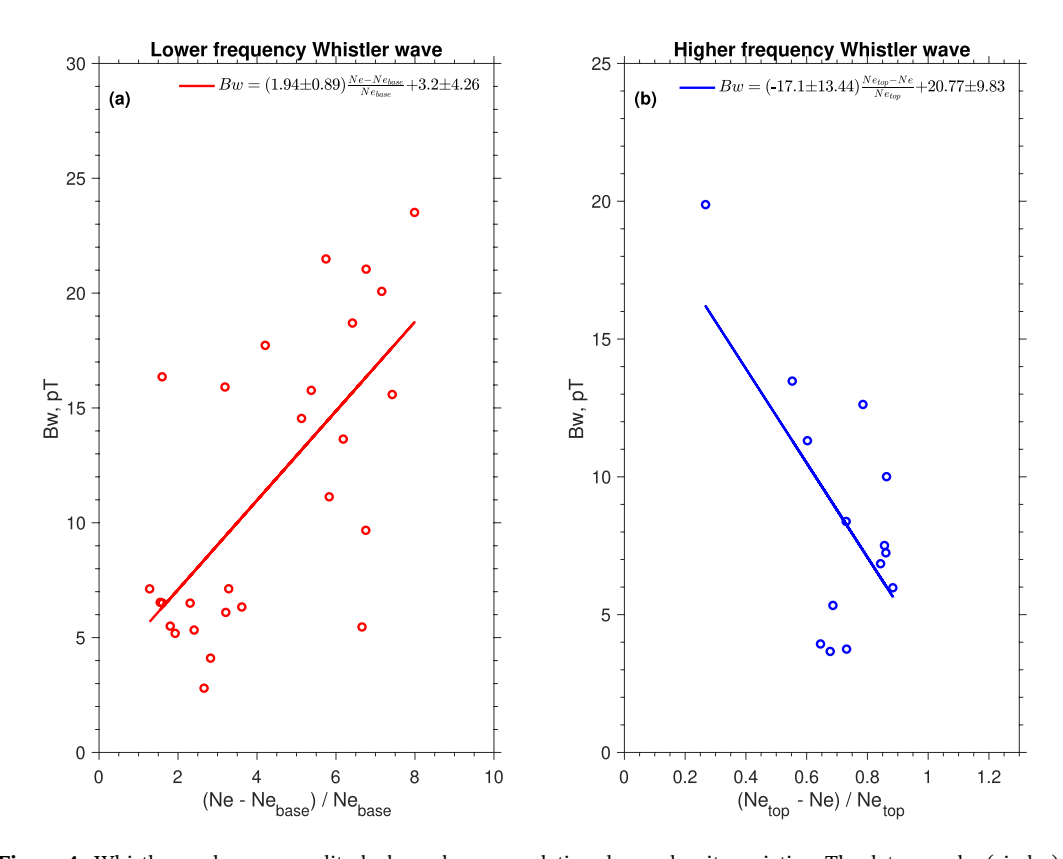


Figure 4. Whistler-mode wave amplitude dependence on relative plasma density variation. The data samples (circles) and linear fitting (straight lines) for (a) lower-frequency whistler-mode waves and (b) higher-frequency whistler-mode waves. The correlation coefficients corresponding to these two fittings are 0.6672 and -0.6248, respectively.

- 1. Density irregularities usually occur near the plasmapause when plasmasphere erosion and refilling occur alternately due to a variation in geomagnetic activity, especially in a geomagnetic storm or substorm.
- 2. The whistler-mode wave intensity shows frequency-dependent modulations with higher-frequency waves ($\sim 0.5 f_{ce}$) concentrated at density troughs and lower-frequency waves ($< f_{lhr}$) concentrated at density crests.
- 3. The modulations of the whistler-mode waves are formed primarily due to wave trapping by density irregularities. The higher-frequency whistler-mode waves are trapped in density troughs due to the small wave refractive index near the parallel direction, while lower-frequency whistler-mode waves are trapped in density crests due to the maximum wave refractive index along the parallel direction.
- 4. Density variations can quantitatively control the whistler-mode wave amplitude. The wave amplitude is correlated (anti-correlated) with the relative density variation amplitude for lower- (higher-) frequency whistler-mode waves.

During a geomagnetic storm, the plasmasphere experiences faster erosion on the time scale of hours due to enhanced convection during the main phase, followed by gradual refilling over a time scale of days (Gallagher et al., 2021). For the storm event presented in this study, density irregularities are found during the recovery phase, while no density irregularity is found during the main phase, when plasmasphere erosion is dominant over the refilling process. These results suggest that density irregularities occur preferentially during the recovery phase, when convection weakens so that the difference between the time scales of convection and refilling decreases.

The modulation of the whistler-mode wave intensity by density irregularities is a common phenomenon in the Earth's inner magnetosphere. For example, during the geomagnetic storm event presented in this study, both VAPs observe the enhancement of lower-frequency whistler-mode wave amplitude in density crests on Orbits 4, 6, 10, and 14. VAP-B observes both lower- and higher-frequency whistler-mode waves in density crests and density troughs on Orbit 12, respectively (not shown).

LIU ET AL. 8 of 10



Acknowledgments

We acknowledge the support of NSF

grant 1702805 through the Geospace

Environment Modeling program and

NASA grants 80NSSC19K0282 and

80NSSC21K0728. R. B. Horne was

supported by NERC Highlight Topic

Grant NE/P01738X/1 (Rad-Sat) and

NERC grant NE/V00249X/1 (Sat-Risk).

We acknowledge the Van Allen Probes

EMFISIS data obtained from https://

emfisis.physics.uiowa.edu/data/index

and HOPE data obtained from https://

cdaweb.gsfc.nasa.gov/index.html.

Density irregularities can regulate the propagation paths of whistler-mode waves and thus confine the wave power inside density crest/trough regions. Thus, stronger density deviations can trap more wave power, which is revealed by the correlation (anti-correlation) between the wave amplitude and relative density variation.

Our results show a strong physical connection among geomagnetic activity, plasmasphere dynamics, and whistler-mode wave dynamics. Density irregularities can control the occurrence and frequency of whistler-mode waves. Furthermore, as shown in our study, there is a quantitative relation between the amplitude of density irregularities and the amplitude of whistler-mode waves. Since whistler-mode waves play important roles in radiation belt electron acceleration and loss, the effects of density irregularities will be of direct relevance. Thus, we suggest that density irregularities should be considered in a physical plasmasphere model, whistler-mode wave model, and radiation belt model.

Data Availability Statement

The Kp, AE, and Dst indices are provided by the WDC for Geomagnetism, Kyoto (http://wdc.kugi.kyoto-u.ac.jp/wdc/Sec3.html). The instability analysis and ray-tracing simulation data are available at this site (https://doi.org/10.5281/zenodo.4556416).

References

Bortnik, J., Chen, L., Li, W., Thorne, R. M., & Horne, R. B. (2011). Modeling the evolution of chorus waves into plasmaspheric hiss. *Journal of Geophysical Research*, 116, 8221. https://doi.org/10.1029/2011JA016499

Cao, J., Liu, Z., Yang, J., Yian, C., Wang, Z., Zhang, X., et al. (2005). First results of low frequency electromagnetic wave detector of tc-2/double star program. *Annales Geophysicae*, 23(8), 2803–2811. https://doi.org/10.5194/angeo-23-2803-2005

Carpenter, D. L., & Anderson, R. R. (1992). An ISEE/Whistler model of equatorial electron density in the magnetosphere. *Journal of Geophysical Research*, 97(A2), 1097–1108. https://doi.org/10.1029/91ja01548

Carpenter, D. L., Anderson, R. R., Calvert, W., & Moldwin, M. B. (2000). Crres observations of density cavities inside the plasmasphere. Journal of Geophysical Research, 105(A10), 23323–23338. https://doi.org/10.1029/2000JA000013

Chen, L., Bortnik, J., Li, W., Thorne, R. M., & Horne, R. B. (2012a). Modeling the properties of plasmaspheric hiss: 1. Dependence on chorus wave emission. *Journal of Geophysical Research*, 117(A5), A05201. https://doi.org/10.1029/2011JA017201

Chen, L., Bortnik, J., Li, W., Thorne, R. M., & Horne, R. B. (2012b). Modeling the properties of plasmaspheric hiss: 2. Dependence on the plasma density distribution. *Journal of Geophysical Research*, 117(A5), A05202. https://doi.org/10.1029/2011JA017202

Chen, L., Thorne, R. M., & Horne, R. B. (2009). Simulation of EMIC wave excitation in a model magnetosphere including structured

high-density plumes. *Journal of Geophysical Research*, 114, 7221. https://doi.org/10.1029/2009JA014204
Chen, L., Thorne, R. M., Jordanova, V. K., & Horne, R. B. (2010). Global simulation of magnetosonic waves instability in the storm time

magnetosphere. *Journal of Geophysical Research*, 115. https://doi.org/10.1029/2010JA015707
Darrouzet, F., Décréau, P. M. E., De Keyser, J., Masson, A., Gallagher, D. L., Santolik, O., et al. (2004). Density structures inside the plasmas-

phere: Cluster observations. *Annales Geophysicae*, 22(7), 2577–2585. https://doi.org/10.5194/angeo-22-2577-2004

Darrouzet, F., Pierrard, V., Benck, S., Lointier, G., Cabrera, J., Borremans, K., et al. (2013). Links between the plasmapause and the radiation belt boundaries as observed by the instruments cis, rapid, and whisper onboard cluster. *Journal of Geophysical Research: Space Physics*, 118(7), 4176–4188. https://doi.org/10.1002/jgra.50239

Forsyth, C., Rae, I. J., Coxon, J. C., Freeman, M. P., Jackman, C. M., Gjerloev, J., & Fazakerley, A. N. (2015). A new technique for determining substorm onsets and phases from indices of the electrojet (sophie). *Journal of Geophysical Research: Space Physics*, 120(12), 10592–10606. https://doi.org/10.1002/2015JA021343

Funsten, H. O., Skoug, R. M., Guthrie, A. A., MacDonald, E. A., Baldonado, J. R., Harper, R. W., et al. (2014). Helium, oxygen, proton, and electron (hope) mass spectrometer for the radiation belt storm probes mission. In N. Fox, & J. L. Burch (Eds.), *The van allen probes mission* (pp. 423–484). Springer US. https://doi.org/10.1007/978-1-4899-7433-4_13

Gallagher, D. L., Comfort, R. H., Katus, R. M., Sandel, B. R., Fung, S. F., & Adrian, M. L. (2021). The breathing plasmasphere: Erosion and refilling. *Journal of Geophysical Research: Space Physics*, 126(4), e2020JA028727. https://doi.org/10.1029/2020JA028727

Grebowsky, J. M. (1970). Model study of plasmapause motion. Journal of Geophysical Research, 75, 4329–4333. https://doi.org/10.1029/JA075i022p04329

 $He, Z., Chen, L., Liu, X., Zhu, H., Liu, S., Gao, Z., \& Cao, Y. (2019). Local generation of high-frequency plasmaspheric hiss observed by van Allen probes. \\ \textit{Geophysical Research Letters}, 46(3), 1141-1148. \\ \text{https://doi.org/10.1029/2018GL081578}$

Horne, R. B. (1989). Path-integrated growth of electrostatic waves: The generation of terrestrial myriametric radiation. *Journal of Geophysical Research*, 94(A7), 8895–8909. https://doi.org/10.1029/ja094ia07p08895

Horne, R. B., Kersten, T., Glauert, S. A., Meredith, N. P., Boscher, D., Sicard-Piet, A., et al. (2013). A new diffusion matrix for whistler mode chorus waves. *Journal of Geophysical Research: Space Physics*, 118(10), 6302–6318. https://doi.org/10.1002/jgra.50594

Jordanova, V. K., Thorne, R. M., Li, W., & Miashi, Y. (2010). Excitation of whistler-mode chorus from global ring current simulations. Journal of Geophysical Research, 115, A00F10. https://doi.org/10.1029/2009JA014810

Kazama, Y., Kojima, H., Miyoshi, Y., Kasahara, Y., Usui, H., Wang, B.-J., et al. (2018). Density depletions associated with enhancements of electron cyclotron harmonic emissions: An erg observation. Geophysical Research Letters, 45(19), 10075–10083. https://doi.org/10.1029/2018GL080117

Kletzing, C. A., Kurth, W. S., Acuna, M., MacDowall, R. J., Torbert, R. B., Averkamp, T., et al. (2013). The electric and magnetic field instrument suite and integrated science (emfisis) on rbsp. Space Science Reviews, 179(1), 127–181. https://doi.org/10.1007/s11214-013-9993-6

LIU ET AL. 9 of 10



- Li, W., Thorne, R. M., Angelopoulos, V., Bortnik, J., Cully, C. M., Ni, B., et al. (2009). Global distribution of whistler-mode chorus waves observed on the THEMIS spacecraft. *Geophysical Research Letters*, 36, L09104. https://doi.org/10.1029/2009GL037595
- Liu, X., & Chen, L. (2019). Instability in a relativistic magnetized plasma. *Physics of Plasmas*, 26(4), 042902. https://doi.org/10.1063/1.5089749 Liu, X., Chen, L., Engel, M. A., & Jordanova, V. K. (2020). Global simulation of electron cyclotron harmonic wave instability in a storm-time magnetosphere. *Geophysical Research Letters*, 47(6). https://doi.org/10.1029/2019GL086368
- Liu, X., Chen, L., & Xia, Z. (2020). The relation between electron cyclotron harmonic waves and plasmapause: Case and statistical studies. Geophysical Research Letters, 47(9). https://doi.org/10.1029/2020GL087365
- Liu, X., Chen, L., Yang, L., Xia, Z., & Malaspina, D. M. (2018). One-dimensional full wave simulation of equatorial magnetosonic wave propagation in an inhomogeneous magnetosphere. *Journal of Geophysical Research: Space Physics*, 123(1), 587–599. https://doi.org/10.1002/2017JA024336
- Liu, X., Liu, W., Cao, J. B., Fu, H. S., Yu, J., & Li, X. (2015). Dynamic plasmapause model based on themis measurements. *Journal of Geophysical Research: Space Physics*, 120(12), 10543–10556. https://doi.org/10.1002/2015JA021801
- Lorentzen, K. R., Blake, J. B., Inan, U. S., & Bortnik, J. (2001). Observations of relativistic electron microbursts in association with VLF chorus. *Journal of Geophysical Research*, 106, 6017–6028. https://doi.org/10.1029/2000JA003018
- Ma, Q., Li, W., Chen, L., Thorne, R. M., Kletzing, C. A., Kurth, W. S., et al. (2014). The trapping of equatorial magnetosonic waves in the Earth's outer plasmasphere. *Geophysical Research Letters*, 41(18), 6307–6313. https://doi.org/10.1002/2014GL061414
- Ma, Q., Li, W., Thorne, R. M., Bortnik, J., Kletzing, C. A., Kurth, W. S., & Hospodarsky, G. B. (2016). Electron scattering by magnetosonic waves in the inner magnetosphere. *Journal of Geophysical Research: Space Physics*, 121(1), 274–285. https://doi.org/10.1002/2015JA021992
- Meredith, N. P., Horne, R. B., Glauert, S. A., Baker, D. N., Kanekal, S. G., & Albert, J. M. (2009). Relativistic electron loss timescales in the slot region. *Journal of Geophysical Research*, 114, A03222. https://doi.org/10.1029/2008JA013889
- Moldwin, M. B., Downward, L., Rassoul, H. K., Amin, R., & Anderson, R. R. (2002). A new model of the location of the plasmapause: CRRES results. *Journal of Geophysical Research*. 107, 1339. https://doi.org/10.1029/2001JA009211
- Santolík, O., Nemec, F., Gereová, K., Macúšová, E., Conchy, Y., & Cornilleau-Wehrlin, N. (2004). Systematic analysis of equatorial noise below the lower hybrid frequency. *Annales Geophysicae*, 22, 2587–2595. https://doi.org/10.5194/angeo-22-2587-2004
- Smith, R. L., Helliwell, R. A., & Yabroff, I. W. (1960). A theory of trapping of whistlers in field-aligned columns of enhanced ionization. Journal of Geophysical Research, 65(3), 815–823. https://doi.org/10.1029/JZ065i003p00815
- Thorne, R. M., Smith, E. J., Burton, R. K., & Holzer, R. E. (1973). Plasmaspheric hiss. *Journal of Geophysical Research*, 78, 1581–1596. https://doi.org/10.1029/JA078i010p01581
- Yu, J., Li, L. Y., Cao, J. B., Chen, L., Wang, J., & Yang, J. (2017). Propagation characteristics of plasmaspheric hiss: Van Allen probe observations and global empirical models. *Journal of Geophysical Research: Space Physics*, 122(4), 4156–4167. https://doi.org/10.1002/2016JA023372
- Yuan, Z., Yu, X., Ouyang, Z., Yao, F., Huang, S., & Funsten, H. O. (2019). Simultaneous trapping of electromagnetic ion cyclotron and magnetosonic waves by background plasmas. *Journal of Geophysical Research: Space Physics*, 124(3), 1635–1643. https://doi. org/10.1029/2018JA026149
- Yue, C., Ma, Q., Jun, C.-W., Bortnik, J., Zong, Q., Zhou, X., et al. (2020). The modulation of plasma and waves by background electron density irregularities in the inner magnetosphere. Geophysical Research Letters, 47(15), e2020GL088855. https://doi.org/10.1029/2020GL088855

LIU ET AL. 10 of 10